

pubs.acs.org/JACS Article

Dynamic Evolution from Single-Atom Catalysts to Active Nanograins for CO₂ Reduction

Juhyung Choi, Sungin Kim, Ji Yong Choi, Sejin Park, Kwanghwi Je, Shikai Liu, Jiahong Jiang, Shaojinlin Yang, Christopher J. Pollock, Rafael Guzman-Soriano, Kathryn Bairley, Bayu I. Z. Ahmad, Phillip J. Milner, Erik H. Thiede, Yun Jeong Hwang, Jihye Park, and Yao Yang*



Cite This: https://doi.org/10.1021/jacs.5c14123



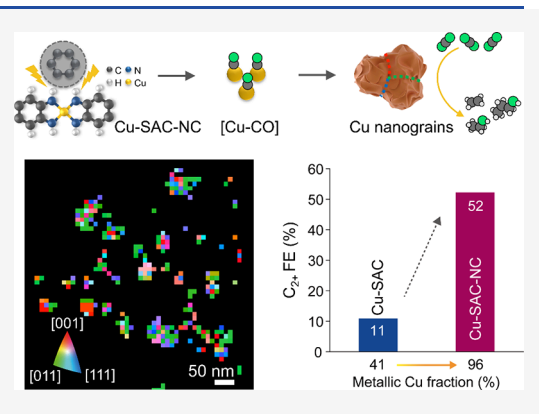
ACCESS

III Metrics & More

Article Recommendations

Supporting Information

ABSTRACT: Understanding dynamic catalyst evolution, particularly Cu-based single-atom catalysts, faces tremendous challenges of tracking rapid and nanoscale evolution and uncontrolled catalyst reoxidation during post-reaction air exposure. Although ex situ/in situ studies have indirectly indicated the structural reconstruction of single-atom catalysts, direct probing of single-atom catalyst evolution requires time-resolved nanoscale operando methods. Here, we present direct experimental evidence of dynamic evolution from single-atom catalysts to Cu nanostructures rich in active nanograins, based on a conductive metal—organic framework-based Cu single-atom catalyst (Cu-SAC). Operando synchrotron-based high-energy-resolution X-ray spectroscopy and IR absorption spectroscopy quantitatively tracked the structural and molecular finger-prints during single-atom-to-nanograin evolution. Cu-SAC supported on nanocarbon (Cu-SAC-NC) with nearly 100% metallic Cu nanograins achieved



a 5-fold increase in multicarbon Faradaic efficiency (C_{2+} FE), relative to the Cu-SAC control group with less than half metallic Cu nanograins. Cu-SAC-NC, with superior electronic conductivity provided by the nanocarbon, facilitated the formation of dense copper carbonyl (Cu-CO) intermediates, leading to a larger fraction of active metallic Cu nanograins for effective C-C coupling and significantly enhanced C_{2+} selectivity. *Operando* electrochemical liquid-cell scanning transmission electron microscopy (EC-STEM) directly captured real-time movies of dynamic structure evolution from isolated Cu single atoms to metallic Cu nanograins under the CO_2RR . *Operando* electrochemical four-dimensional (4D) STEM reveals the complex polycrystalline Cu nanostructures rich in metallic nanograin boundaries, serving as catalytically active sites. This study paves the way for the design of a new generation of single-atom catalysts based on their *operando* active structures instead of pristine structures.

INTRODUCTION

One of the grand challenges of catalysts is identifying the active sites and capturing real-time "movies" of catalytic processes, i.e., watching catalysis in action. 1-4 It is increasingly evident that pristine and post-mortem electrocatalysts, characterized ex situ, most likely do not maintain the same active structures, particularly under strong electrochemical driving force (strongly reducing/oxidizing potentials), such as CO_2 reduction to liquid fuels, $^{5-9}$ N_2 or NO_3^- reduction to NH₃, 10-12 oxygen reduction/evolution reactions in fuel cells/ water electrolyzers, 1,13-17 or organic electrosynthesis. 18-20 The need to establish structure—(re)activity correlations in electrocatalysis motivates the development of operando (operating) and in situ (on-site) methods. 21-23 Electrochemical CO2 reduction reaction (CO2RR) with renewable energy has emerged as a key technology to produce value-added chemicals and fuels with the potential to close the carbon cycle. Copper (Cu)-based electrocatalysts are well-known for their unique ability to promote C-C coupling reactions, which influences the multicarbon (C_{2+}) product activity/selectivity. A previous

study reveals that sub-10 nm Cu nanoparticles (NPs) undergo dynamic structural evolution into metallic Cu nanograins under CO₂RR via electrochemical reconstruction, with the resulting nanoscale grain (nanograin) boundaries serving as active sites for C–C coupling.² More recent studies employing Cu-based nanocube and nanowire catalysts revealed size-dependent formation kinetics of nanograins from nanocubes, driven by the migration of Cu–CO (copper–carbonyl) species.^{24,25}

Single-atom catalysts have emerged as an important family of catalysts for the CO₂RR due to the atomic-level control of the identity and density of the metal center and molecular tunability of supported structures with N, O, C, or other

Received: August 14, 2025 Revised: September 19, 2025 Accepted: September 22, 2025



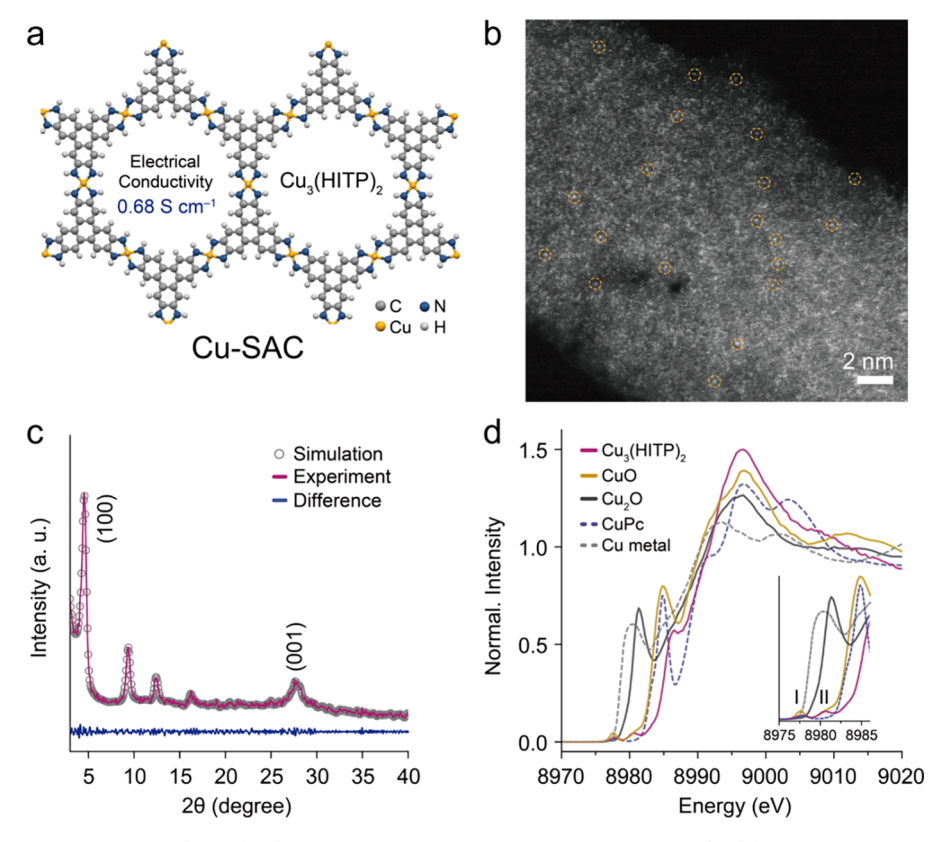


Figure 1. (a) Structure scheme of $Cu_3(HITP)_2$ (denoted as Cu single-atom catalyst, Cu-SAC), (b) Atomic-scale HAADF-STEM images of $Cu_3(HITP)_2$ with selected Cu atoms highlighted in dashed yellow circle, (c) Experimental and simulated X-ray diffraction patterns, and (d) HERFD XAS spectra of $Cu_3(HITP)_2$ along with the spectra of various references.

neighboring atoms. Several early ex situ or in situ studies indicated that Cu-single-atom catalysts experienced structural reconstruction under CO2 electrolysis, wherein isolated Cu sites convert into few-atom Cu clusters or metallic Cu nanoparticles. 26-29 For instance, in situ attenuated total reflection surface enhanced infrared absorption spectroscopy (ATR-SEIRAS) analysis of Cu-single-atom catalysts supported on C₃N₄ catalysts confirmed the evolution toward metallic Cu, identified as the active phase for C₂₊ product formation.²⁸ However, the carbon structures in these studies are typically low-crystallinity N-doped carbon networks derived from hightemperature pyrolysis. The presence of various nitrogen configurations in such structures results in a heterogeneous Cu-N coordination environment, making it challenging to identify the origin of the structural evolution. 30,31 Another class of Cu-single-atom catalyst features well-defined Cu-N coordination structures, as found in crystalline organic molecules such as Cu phthalocyanine (CuPc). 26,27,32,33 These molecular-based Cu single-atom catalysts inherently show poor electrical conductivity, which typically requires the addition of conductive nanocarbon support. A shift in the product selectivity ratio of C_{2+} to C_1 products has been observed depending on the mixing ratio between CuPc and commercial carbon, such as Vulcan XC-72 carbon (VC). 32,33 This indicates that nanocarbons not only enhance conductivity but also may play a role in tuning catalytic selectivity. Therefore, constructing well-ordered conductive Cu-single-atom catalysts would allow for a more systematic investigation of the structural evolution and the role of nanocarbon during CO₂RR.

 ${\rm Cu_3(HITP)_2}$ (HITP = 2,3,6,7,10,11-hexaiminotriphenylene) is a well-known conductive metal—organic framework (MOF), where a single Cu atom is coordinated in a square-planar geometry with ${\rm N_4}$ sites.³⁴ Owing to its high electrical conductivity and chemical stability, it has been widely employed in electrochemical applications, including energy storage and conversion reactions.^{35–37} Although previous *ex situ* and *in situ* studies reported the application of ${\rm Cu_3(HITP)_2}$ in ${\rm CO_2RR}$,³⁷ the direct probing of single-atom-to-nanograin evolution of this type of catalyst remains unexplored. These properties make ${\rm Cu_3(HITP)_2}$ a model system for investigating the structural evolution kinetics and active sites under the ${\rm CO_2RR}$.

Herein, we designed Cu₃(HITP)₂ as a model single-atom catalyst (denoted as Cu-SAC) for the CO₂RR and compared it with a Cu₃(HITP)₂ electrode physically mixed with nanocarbon (denoted as Cu-SAC-NC) to investigate structureactivity relationships. The CO₂RR performance of Cu-SAC-NC showed a significantly enhanced Faradaic efficiency (FE) for C_{2+} products, reaching more than 50%, compared to ~10% for Cu-SAC. Our multimodal operando approaches, including high-energy-resolution X-ray absorption spectroscopy (XAS) and ATR-SEIRAS, observed the faster structural evolution of Cu-SAC-NC forming a large fraction of metallic Cu nanograins compared with Cu-SAC. Furthermore, operando electrochemical liquid-cell scanning transmission electron microscopy (EC-STEM) and four-dimensional STEM (4D-STEM) analyses of Cu-SAC-NC demonstrated the migration of Cu-CO species and their growth into polycrystalline Cu with various nanograin boundaries, which serve as active sites for C–C coupling. Our study underscores the dynamic structural

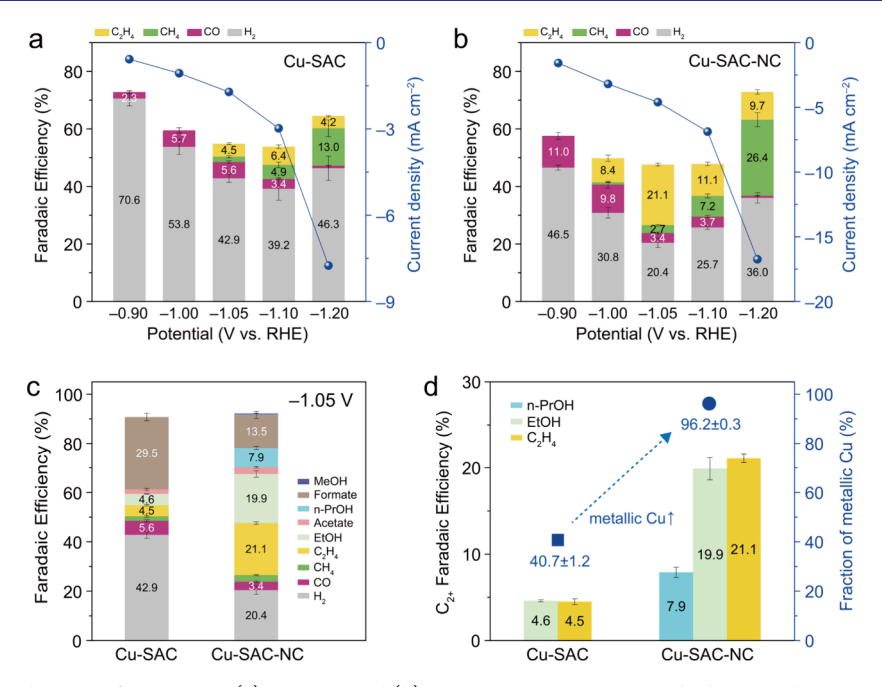


Figure 2. Gas product distributions of CO_2RR on (a) Cu-SAC and (b) Cu-SAC-NC at various applied potentials in CO_2 -saturated 0.1 M KHCO₃. (c) All product distributions of both catalysts at an applied potential of -1.05 V vs RHE with iR correction and (d) Structure—activity correlations of major C_{2+} products (n-PrOH, EtOH, and C_2H_4) distributions and quantitative X-ray analysis of the relative fraction of metallic Cu for both catalysts at -1.05 V vs RHE with iR correction.

evolution of Cu single atoms as a key factor in C–C coupling activity and provides new insight into the role of carbon support under the CO_2RR .

■ RESULTS AND DISCUSSION

To systematically investigate the dynamic structural evolution of Cu single-atom catalysts (Cu-SAC) during the CO₂RR, we focused on developing a Cu-SAC model system which has two key properties: (1) a well-defined Cu-N binding structure and (2) high electrical conductivity for the CO₂RR. To this end, we synthesized electrically conductive metal-organic frameworks (MOFs) based on a conjugated linker, HATP (HATP = 2,3,6,7,10,11-hexaaminotriphenylene). First, the HATP linker, coordinated with the Cu²⁺ metal node, was used to construct Cu₃(HITP)₂ (HITP: 2,3,6,7,10,11-hexaiminotriphenylene) as the model Cu-SAC.³⁸ The linker was confirmed by ¹H NMR (Figure S1). Schematic illustration presented in Figure 1a indicates a two-dimensional molecular structure linked by Cu²⁺ ions with a square planar coordination geometry, and its inplane d-p conjugation between HITP ligands and Cu nodes enables effective charge transport. Cu₃(HITP)₂ exhibits an electrical conductivity of 0.68 S cm⁻¹ via the four-point probe method at room temperature, which is comparable to that of conventional Cu-based electrocatalysts (Cu₂O or CuO films).³⁹ As shown in Figure S2, bright-field transmission electron microscopy (TEM) images of Cu₃(HITP)₂ show the nanorod-like structure. The presence of Cu atoms is further verified by an atomic-scale high-angle annular dark-field scanning transmission electron microscopy (HADDF-STEM) image, where individual Cu atoms (marked in dashed yellow circles) clearly exist in the MOF structure in Figure 1b. The high crystallinity of Cu₃(HITP)₂ was investigated by powder X-ray diffraction pattern (XRD) analysis and refined using the Pawley fit. The experimental XRD pattern matched well with the simulated structure, with an R_{wp} of 3.89%, suggesting a well-defined single-phase structure (Figure 1c). Cu₃(HITP)₂

shows sharp diffraction patterns and two peaks at 4.56° and 27.6°, which are ascribed to the (100) and (001) planes, respectively, confirming the 2D stacked structure. High energyresolution fluorescence-detected (HERFD) XAS was conducted to further provide the coordination environment of $Cu_3(HITP)_2$. HERFD XAS detects $Cu\ K_{\alpha 1}$ emission lines and enables resolution of the pre-edge features in X-ray absorption near-edge structure (XANES) with a much higher energy resolution (ca. 0.5 eV) than conventional XAS (ca. 1.5 eV) in fluorescence mode. 40-42 Highly sensitive HERFD XANES of Cu₃(HITP)₂ shows two distinct peaks in the adsorption regions (Figure 1d, inset). A pre-edge peak I, which overlaps with the CuPc feature at 8978.0 eV, is characteristic of Cu²⁺-N coordination, and a near-edge peak II at 8980.5 eV, located between the Cu metal and Cu₂O features, suggests Cu^{0/+} oxidation states that are possibly due to defects in the HITP ligand. 34,43 As shown in Figure S3, extended X-ray absorption fine structure (EXAFS) shows a peak at R+ Δ 1.44 Å, corresponding to the Cu-N bond of Cu₃(HITP)₂. Furthermore, the high-resolution XPS Cu 2p_{3/2} spectrum of Cu₃(HITP)₂ shows a peak at 932.8 eV, which is associated with Cu^{0/+} species, and another peak at 934.7 eV, which is attributed to Cu²⁺ species (Figure S4a). High-resolution X-ray photoelectron spectroscopy (XPS) spectra of C 1s and N 1s also confirm the intact conjugated structure of the HITP linker within the framework (Figures S4b and 4c). Overall, these results demonstrate the highly ordered and electrically conductive nature of Cu₃(HITP)₂ as a pristine single-atom catalyst (Cu-SAC).

Electrochemical CO₂ reduction reaction (CO₂RR) of Cu-SAC was carried out in an H-cell system, and we further fabricated an electrode consisting of Cu-SAC and nanocarbon support (*denoted as* Cu-SAC-NC, see Experimental section for detailed information on nanocarbon). Scanning electron microscopy (SEM) images of the Cu-SAC-NC electrode show a well-dispersed physical mixture of nanocarbon and Cu-

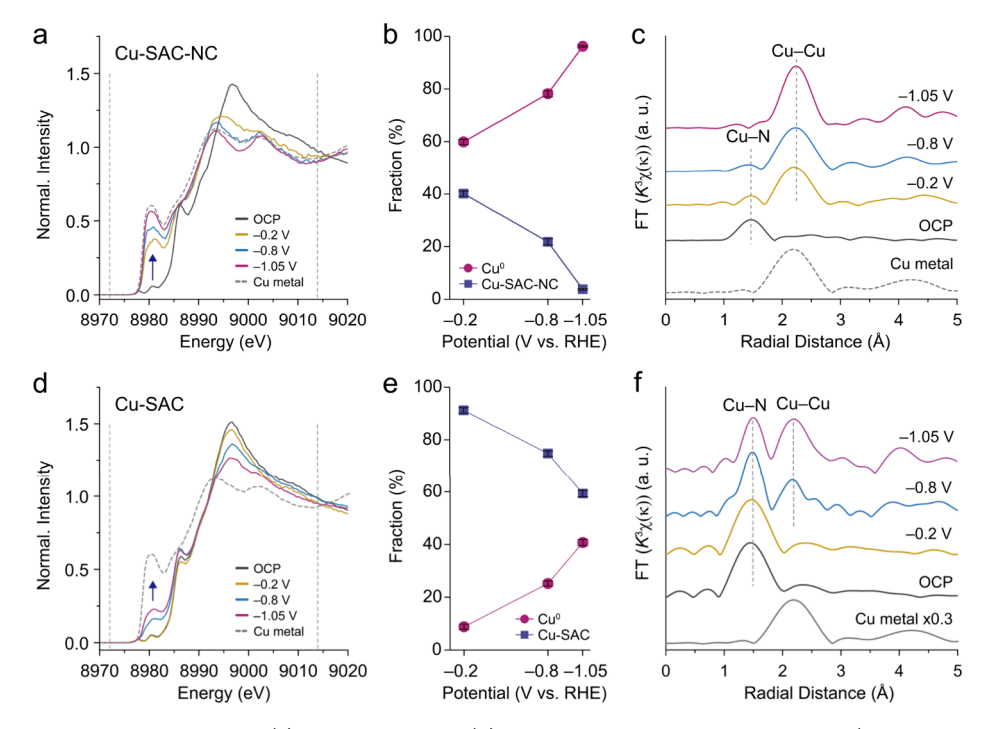


Figure 3. Operando HERFD XANES spectra of (a) Cu-SAC-NC and (d) Cu-SAC at various applied potentials (the dashed vertical lines mark the range of the LCF analysis). Quantitative valence state analysis of the relative fraction of metallic Cu of (b) Cu-SAC-NC and (e) Cu-SAC. Operando EXAFS spectra of (c) Cu-SAC-NC and (f) Cu-SAC at various applied potentials.

SAC (indicated by a white arrow) in Figure S5. Furthermore, TEM images of Cu-SAC-NC indicate that Cu-SAC and NC are well mixed at the nanoscale, forming numerous intimate interfaces (Figure S6). These thin mixture layers observed in TEM images, which stack into multilayer structures on the Cu-SAC-NC electrode, are consistent with the morphology observed in SEM images. HERFD XAS of Cu-SAC-NC shows the pronounced white line at 8996.7 eV (marked as A), which appears along with the enhanced ligand effect manifested as peak B at 8986.5 eV (Figure S7a).44 The slightly lower intensity observed at peaks A and B for Cu-SAC-NC compared to Cu-SAC suggests that the π - π interaction between the Cu²⁺ and the nanocarbon enhances the core-hole screening effect.⁴⁵ However, the near-edge region of both catalysts shows nearly the same characteristic spectra, indicating that the physical mixing with NC does not change the chemical state or electronic structure of Cu (Figure S7b). CO₂RR performances were measured in 0.1 M KHCO₃ electrolyte at the potential ranges of -0.90 to -1.20 V vs reversible hydrogen electrode (RHE) (Figure 2a and 2b). All potentials are referred to the RHE scale, unless otherwise noted.

As the applied potential changed from -0.90 to -1.20 V, the total current density increased from -1.6 to -16.7 mA cm⁻², while the FE of C_2H_4 showed a nonmonotonic change. The Cu-SAC-NC revealed the highest FE for C_2H_4 of 21.1% at -1.05 V, significantly higher than that of Cu-SAC (4.5%) under the same potential. Cu-SAC-NC also exhibits a higher current density of 4.6 mA cm⁻² compared to Cu-SAC (1.71 mA cm⁻²). Figure 2c shows that the total C_{2+} FE of Cu-SAC-NC reaches 51.6% at -1.05 V, higher than that of Cu-SAC (10.9%). These results imply that the enhanced C–C coupling reactions observed for Cu-SAC-NC cannot be simply explained by the improved charge transport of Cu-SAC arising from the nanocarbon matrix. As further shown in Figure 2d,

the major C_{2+} product yield of Cu-SAC-NC is increased by more than 5.4 times compared to that of Cu-SAC. The C_{2+} FE performance of Cu-SAC-NC is among the highest in Cu-based single-atom catalysts and is comparable to Cu nanoparticle-derived nanograin catalysts (Table S1). Linear combination fitting (LCF) analysis, determined by *operando* HERFD XANES, was performed for quantification of the relative fraction of metallic Cu. The LCF results indicate that Cu-SAC-NC exhibits a higher fraction of metallic Cu of 96.2% \pm 0.3% at -1.05 V compared to that of Cu-SAC (40.7% \pm 1.2%). This suggests that the enhanced C_{2+} selectivity could be explained by the higher fraction of metallic Cu, which will be discussed in detail (*vide infra*).

Operando HERFD XAS reveals the dynamic structural evolution kinetics for Cu single atoms under the CO₂RR as the applied potential increases from -0.2 to -1.05 V (Figure 3). Operando HERFD XANES spectra of Cu-SAC-NC show a pronounced peak corresponding to metallic Cu, which emerges at around 8980 eV at an applied potential of -0.2 V (Figure 3a). It becomes more prominent with increasing potential and is accompanied by an increase in the postedge at around 9024 eV (Figure S8a). The LCF results of the relative metallic Cu content indicate that the structural evolution kinetics are rapid, with 59.9% metallic Cu formed at −0.2 V and reaching up to 96.2% at −1.05 V in Figure 3b. The corresponding Fourier transform k^3 -weighted extended X-ray absorption fine structure (EXAFS) analysis further reveals a distinct Cu-Cu peak for metallic Cu at 2.2 Å (radial distance with no phase correction) at -0.2 V (Figure 3c). Moreover, the scattering of Cu-N is absent at −1.05 V, indicating a nearly complete structural evolution from Cu-SAC to metallic Cu nanograins, consistent with the XANES quantification (Figure 3c). However, Cu-SAC shows a slower rate of structural evolution compared to Cu-SAC-NC, and no observable metallic Cu feature in the postedge region even at -1.05 V (Figures 3d and S8b). The

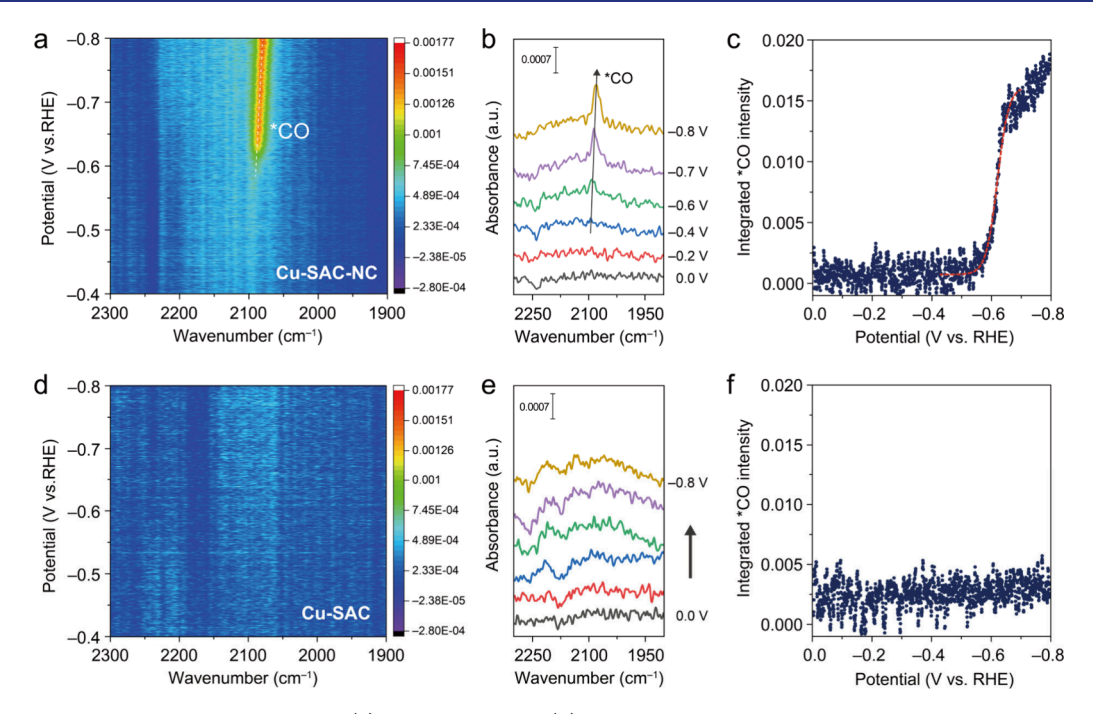


Figure 4. Operando time-resolved ATR-SEIRAS of (a) Cu-SAC-NC and (d) Cu-SAC during the CO_2RR and the ATR-SEIRAS spectra of (b) Cu-SAC-NC and (e) Cu-SAC. Potential-dependent integrated *CO adsorption intensity of (c) Cu-SAC-NC and (f) Cu-SAC.

LCF analysis of Cu-SAC exhibits a modest increase of metallic Cu fraction from 8.8% at -0.2 V to approach only 40.7% at -1.05 V, confirming slow metallic Cu formation from the single atom sites in Figure 3e. This is further supported by the corresponding EXAFS results, which reveal a remaining Cu-N bond at -1.05 V (Figures 3f and S9). Furthermore, the average coordination number (CN) was quantified through the EXAFS fitting process (Table S2). At -1.05 V, the average CN of Cu-SAC-NC shows around 12, comparable to that of bulk Cu. 42 In contrast, the EXAFS fitting of Cu-SAC shows the CN for around 3.0 at -1.05 V (Figure S9). This suggests that fewatom Cu clusters are predominantly formed and that such lowcoordinated clusters are more effective for producing C_1 product or H_2 under CO_2RR . As shown in Figure S10a, the postelectrolysis ex situ HAADF-STEM image of Cu-SAC confirms the presence of sub-1 nm Cu clusters, consistent with the LCF fitting results indicating the formation of a fewnanometer-sized Cu clusters. However, around 6 nm-sized Cu NPs were also observed in the post-CO₂RR Cu-SAC, which are surrounded by the remaining single Cu atoms loosely attached to their surfaces (Figure S10b). This indicates that the active sites for C-C coupling reaction are likely Cu nanoclusters/nanograins rather than pristine Cu-SAC, which is consistent with our recent operando study of metallic Cu nanograins derived from copper phthalocyanine molecular catalysts.²⁴ Furthermore, this study elucidates the formation of polycrystalline Cu nanograins enriched with grain boundaries, which can act as favorable motifs for C-C coupling, leading to C₂₊ products. Therefore, although both Cu-SAC and Cu-SAC-NC undergo structural evolution toward metallic Cu clusters, the higher C_{2+} selectivity of Cu-SAC-NC can be attributed to a larger fraction of metallic Cu nanograins, which serve as abundant active sites for effective C-C coupling reactions.²

Notably, these results suggest that the nanocarbon forming an intimate interface with Cu-SAC significantly influences its dynamic structural evolution under the CO₂RR, highlighting the need for a more detailed mechanistic understanding of the

effect of nanocarbon. If the carbon support itself contributes directly to the formation of metallic Cu, we hypothesized that a similar particle growth pathway would also occur under a N2 atmosphere. Accordingly, Cu-SAC-NC was further observed by operando HERFD XANES to track the structural evolution kinetics under N₂ as shown in Figure S11. A noticeable transformation toward Cu(I) was observed under N₂ condition at the applied potential of -0.2 V. This behavior distinctly contrasts with the CO2RR condition, where CO induces the ejection of single Cu atoms and drives the migration of mobile Cu-CO complexes, leading to the formation of metallic Cu.²⁴ Under N₂ conditions, however, in the absence of CO, the structural evolution is possibly governed by the dissolution/ deposition of Cu ions followed by the formation of surface Cu(I) species. ⁴⁷ At -1.05 V, the LCF fitting extracted from the XANES region shows that Cu-SAC-NC approaches a metallic Cu fraction of 96.9%, which is comparable to the structural evolution observed under CO₂RR. As shown in Figure S12, EXAFS analysis also reveals a distinct Cu-Cu peak corresponding to metallic Cu. A fitted average CN of 11.3 is statistically identical with the CN of 12.0 obtained under CO₂RR within the uncertainty of the EXAFS measurements. In summary, these observations suggest that nanocarbon plays a significant role beyond merely enhancing electronic conductivity. It promotes the formation of a high-concentration Cu-CO complex to facilitate the evolution of metallic Cu clusters into large metallic Cu nanograins.

In situ time-resolved attenuated total reflection surface enhanced infrared absorption spectroscopy (ATR-SEIRAS) analysis was employed to track the electrochemically driven formation of metallic Cu as the applied potential increased (Figure 4). At the onset potential of -0.6 V, the band near 2092 cm⁻¹ observed on Cu-SAC-NC was assigned to atopbound *CO on metallic Cu sites with increasing intensity at more negative potentials (* stands for surface adsorption). It suggests high-density Cu-CO complexes migrations associated with the growth of metallic Cu NPs (Figure 4a-c). ^{24,28}

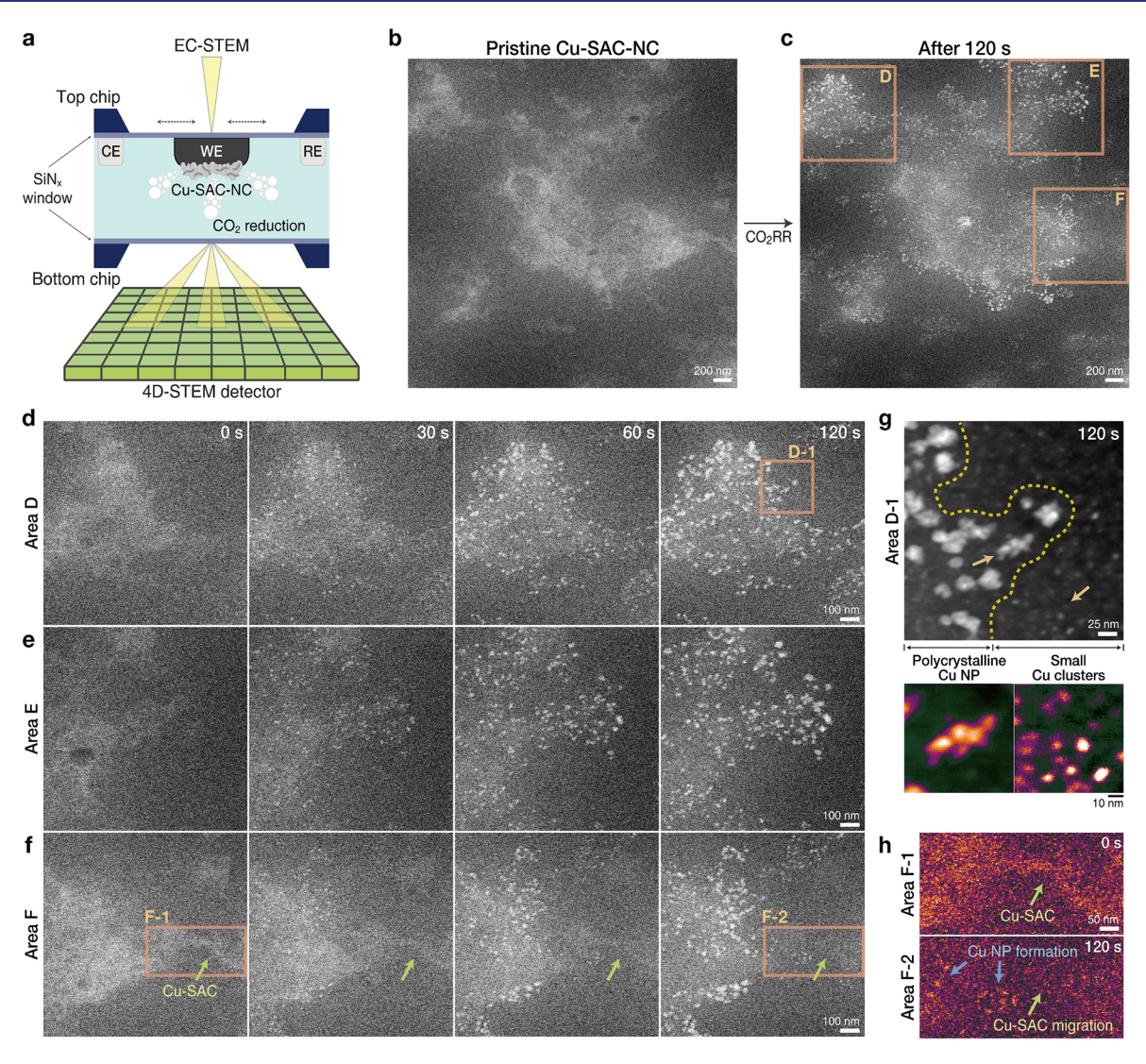


Figure 5. (a) A scheme of operando EC-STEM integrated with 4D-STEM. Low magnification EC-STEM images (b) pristine-SAC and (c) Cu nanograins after the CO₂RR for 120 s in liquids. Selected magnified EC-STEM images during CO₂RR of (d) 'Area D', (e) 'Area E', and (f) 'Area F' indicated by orange boxes in (c). (g) A high magnification EC-STEM image of 'Area D-1' at 120 s indicated by orange boxes in (d). The left and right side of the yellow dashed line displays polycrystalline Cu nanoparticles and numerous small Cu clusters, respectively. At the bottom, the larger Cu nanograins and small Cu clusters, indicated by orange arrows, are displayed as enlarged false-colored images. Enlarged images of larger Cu nanograins at the bottom of (g) are indicated by orange arrows. (h) False-color EC-STEM images of 'Area F-1' and 'Area F-2' indicated by orange boxes in (f).

The red shift of the atop *CO bands from 2092 to 2078 cm⁻¹ in the potential range from -0.6 V to -0.8 V suggested a noticeable Stark effect (70 cm V⁻¹) adsorbed on the catalyst surface.⁴⁸ It is notable that no observable *CO signal appears at the applied potential of -0.2 V, where the formation of metallic Cu from single Cu sites was previously confirmed by operando HERFD XAS. This implies that the detectable atop *CO signal emerges after the formation of larger Cu NPs at the highly applied potential. In contrast, no discernible *CO signal is observed on Cu-SAC, which supports that a distinct CO adsorption band appears once most few-nanometer Cu clusters evolve into larger NPs (Figure 4d-f). In the potential range from -0.6 to -0.8 V, the hydrogen evolution reaction (HER) dominates on both catalysts in Figure S13. Furthermore, the signal near 3500 cm⁻¹ is attributed to interfacial water in the electric double layer (EDL), appearing at 3487 cm⁻¹ for Cu-SAC and 3515 cm⁻¹ for Cu-SAC-NC at 0 V, respectively (Figure S14).⁴⁹ As the potential increases to

-0.8 V, Cu-SAC-NC shows a milder red-shift to 3467 cm⁻¹ in this region, whereas Cu-SAC exhibits a noticeable red shift to 3348 cm⁻¹ and a shoulder peak near 3200 cm⁻¹. The stable interfacial water band in Cu-SAC-NC can be attributed to the influence of the nanocarbon support since the evolution from Cu-SAC to metallic Cu nanograins is also observed by operando HERFD XAS analysis. Furthermore, a control sample, Cu-SAC-NC_{0.1}, was prepared by reducing the nanocarbon content to 0.1 (10%) of that in Cu-SAC-NC. Under CO2RR, a weak *CO intensity was observed at the onset potential of -0.65 V (Figure S15a and S15b), and no obvious shift in the interfacial water band was detected, similar to the feature of Cu-SAC-NC (Figure S15c), supporting that the nanocarbon may contribute to maintaining a stable interfacial water environment. The presence of metallic Cu for C-C coupling reactions was also revealed by the distribution of the CO₂RR product in Figure S15d. To explore whether the high electrical conductivity alone is responsible for

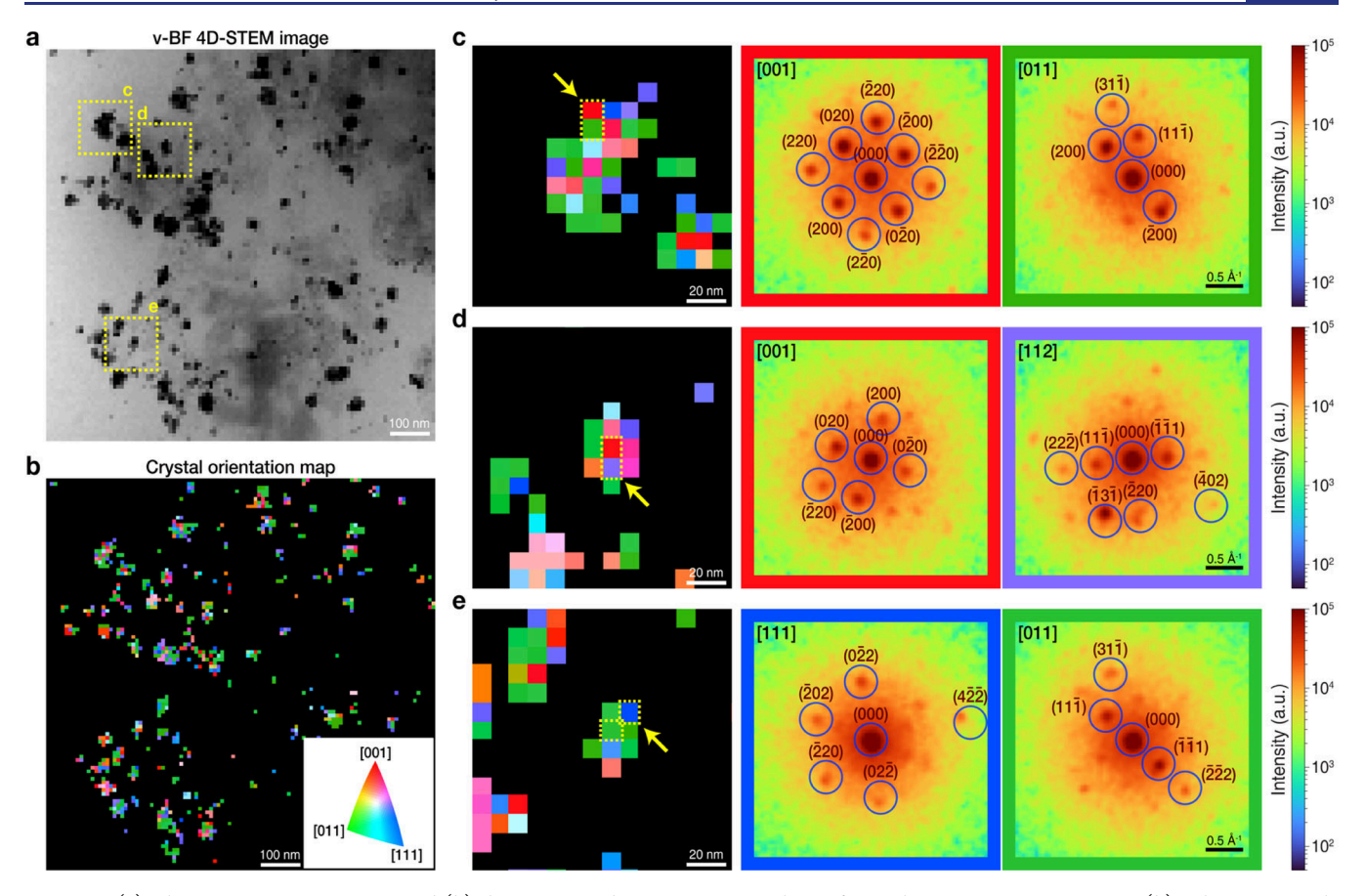


Figure 6. (a) The v-BF 4D-STEM image and (b) the corresponding 4D-STEM analysis of crystal orientation map. Inset in (b): The inverse pole figure of Cu metal. (c-e) Enlarged crystal orientation maps of selected examples of Cu nanograins from areas indicated by yellow dashed boxes in (a). Color-coded diffraction patterns of colored pixels, indicated by yellow arrows and dashed boxes, are presented next to the enlarged maps. Each crystal orientation is indexed at the top-left of the diffraction patterns. Simulated diffraction patterns from the matched orientations are denoted and marked with blue circles.

the formation of metallic Cu from Cu-SAC, we carried out a control experiment using titanium nitride (TiN) NPs with an average size of 20 nm (Figure S16a) as a conductive but CO₂RR-inactive catalyst substrate.⁵⁰ As shown in the gas product distributions (Figure S16b), Cu-SAC-TiN exhibited H₂ FE of over 60% throughout the CO₂RR performances, with low C₂H₄ FE (2.5%) during the CO₂RR for 60 min, in sharp contrast to Cu-SAC-NC with C2H4 FE over 20%. Furthermore, time-resolved ATR-SEIRAS revealed no detectable CO adsorption signals on Cu-SAC-TiN within the applied potential range of -0.4 to -0.8 V vs RHE (Figure S16c and S16d), consistent with the sluggish kinetics of metallic Cu formation. These results suggest that the nanocarbon facilitates the formation of Cu-CO complexes, promoting the evolution of metallic Cu species. However, the effect of interfacial water structures in Cu-CO complex migration kinetics within the EDL and their influence on subsequent particle growth is under current investigation and will be included in our future study.⁵¹⁻⁵³

Operando electrochemical liquid-cell STEM (EC-STEM) was employed to directly capture real-time movies of the structural evolution of Cu-SAC-NC under CO₂RR conditions (Figure 5 and Movie S1). The liquid-cell consisted of a three-electrode system with Cu-SAC-NC deposited on a glassy carbon working electrode (WE) and a Pt counter and a pseudoreference electrode (RE) (Figures 5a and S17). The liquid cell was filled with the CO₂-saturated 0.1 M KHCO₃

electrolyte under electrochemical potentials to simulate the $\rm CO_2RR$ process. This setup was integrated with a four-dimensional STEM (4D-STEM) detector (Figure 5a), which enables the capturing of a 2D electron diffraction pattern at each pixel in a real-space 2D scan of the sample. 4D-STEM, based on the unique electron microscope pixel array detector (EMPAD), achieves single-electron sensitivity and a fast frame rate of 10,000 frames/second. We have demonstrated that 4D-STEM is indispensable for achieving structural mapping of beam-sensitive catalytic active nanostructures in liquid at a low beam dose of 1–10 e-/Ų or lower. S

Operando EC-STEM images clearly show the evolution from Cu-SAC-NC to metallic Cu nanograins with tens of nanometers along the carbon supports during the CO₂RR for 120 s (Figure 5b, 5c). It should be noted that the structural evolution in EC-STEM is accelerated by the stronger electrical field in confined liquid space, relative to hours-long benchtop experiments (Figure S18).24 Consistent with the results of operando HERFD XAS and ex situ STEM analysis, 4D-STEM electron diffraction analysis demonstrated that they are metallic Cu nanoparticles (Figure S19). Closer examination of selected regions shows that the particle sizes gradually increase during the CO₂RR (Figure 5d-f). A higher magnification image of 'Area D-1' at 120 s, in which contrast was enhanced through the machine-learning-based algorithm (Figure S20), 56 captured that numerous few-nm Cu nanoclusters are distributed near the larger particles (Figure 5g).

Moreover, the larger particles exhibit polycrystalline features with rough surfaces and multiple grains (Figure 5g). The representative EC-STEM images at 30, 60, and 120 s, displayed as Figures S21a and S21b, were binarized, allowing for the quantification of time-series structural evolutions. The size distributions of Cu nanoparticles formed from Cu-SAC-NC at each time frame shift toward larger sizes with extended reaction time, indicating the particle growth during CO2RR (Figure S21c), which is supported by the increasing trend of mean particle sizes from ~13 to ~23 nm as the reaction proceeds from 30 to 120 s (Figure S21d). Moreover, the proportion of particles larger than 30 nm substantially increases (Figure S21c). Given that the amount of Cu required for the growth of larger particles increases exponentially, the large particles observed in the histogram at 120 s indicate that the Cu nanoparticles grow through the coalescence of smaller Cu clusters. The decrease in the mean particle circularity at 120 s indicates that particle shapes change from spherical to elliptical or dumbbell-like forms (Figure S21e), supporting particle growth via coalescence (Figure 5g). These findings indicate that the Cu nanograins grow through the coalescence of smaller Cu clusters, resulting in polycrystalline Cu nanoparticles with multigrain structures. Additionally, focused examinations of local regions of 'Area F', where the images were color-coded for enhanced visibility, show that a nanorodlike Cu-SAC is gradually consumed while Cu nanograins are formed in the surrounding area (Figures 5f, 5h, and S22). Operando EC-STEM directly visualizes and complements operando HERFD XAS analysis, where the ejection of single Cu atoms by CO drives the migration of mobile Cu-CO complexes, leading to the formation of metallic Cu nanograins (Figure 3). Consistently, when Cu-SAC-NC was prereduced under N₂ for 60 min prior to CO₂RR, the subsequent C₂H₄ selectivity (FE of 11.7%) of Cu-SAC-NC was lower than that of direct CO₂RR (FE of 21.1%), indicating that nanograins form less effectively under N_2 preconditioning (Figure S23). These results reinforce the idea that the abundant nanograins generated via Cu-CO intermediates under CO2 are critical for driving efficient C-C coupling. To the best of our knowledge, this study represents the first direct nanoscale imaging evidence showing the evolution from single-atom catalysts to active nanostructures under electrochemical conditions.

The 4D-STEM measurement of the liquid-cell enables the crystal orientation mapping of individual metallic Cu nanograins, providing pixelated orientation information on a 2D real-space image (Figure 6). A virtual bright field (v-BF) STEM image was obtained by reconstruction of center disk signals of 2D diffraction patterns where the unscattered beam passed through, which exhibit metallic Cu nanograins with a darker contrast (Figure 6a). Using the 2D diffraction patterns acquired at each pixel of the v-BF image, pixelated crystal orientations of the Cu nanoparticles were obtained through the ACOM package with py4DSTEM (Figure 6b). 57,58 This computational algorithm compares the experimental diffraction patterns with simulated diffraction patterns of Cu metal for all possible orientations to determine the corresponding crystal orientations, which are displayed as distinct colored pixels (see the experimental section for details). In each enlarged crystal orientation map of three local regions, marked with yellow dashed boxes in Figure 6a, diffraction patterns of two adjacent pixels, where the images were color-coded for enhanced visibility, are presented and overlaid with simulated diffraction patterns from the matched crystal orientations (Figure 6c-e).

These enlarged maps clearly reveal that individual Cu nanograins consist of various colored pixels, indicating their polycrystalline feature with multiple nanograins. Note that certain pixels contain overlapping diffraction patterns from multiple orientations, which directly indicate the polycrystalline structures of Cu nanograins (Figure S24).

CONCLUSION

In conclusion, we introduced a well-defined Cu-SAC to systematically investigate the structural-activity relationships under CO2RR conditions through multimodal operando methods. Operando HERFD XAS revealed that Cu-SAC-NC exhibits faster structural evolution kinetics toward metallic Cu than Cu-SAC, forming larger Cu NPs. Combined with operando ATR-SEIRAS, we propose that nanocarbons do not directly promote the growth of metallic Cu but rather facilitate the formation of a high density of Cu-CO (copper carbonyl) complexes, which act as key intermediates for structural evolution. The dynamic migration of Cu-CO complexes and their growth into metallic Cu nanograins were directly captured by operando EC-STEM. Furthermore, 4D-STEM crystal orientation mapping confirmed the formation of numerous polycrystalline Cu nanograin boundaries, which serve as active sites for C-C coupling. Therefore, using correlative operando techniques, this work provided structural and molecular insights into the dynamic structural evolution of the well-defined Cu-SAC and uniquely uncovered the critical role of nanocarbon in forming a larger fraction of nanograin boundaries as key for C-C coupling and resulting in enhanced multicarbon selectivity.

ASSOCIATED CONTENT

Supporting Information

The Supporting Information is available free of charge at https://pubs.acs.org/doi/10.1021/jacs.5c14123.

Supplementary operando movie showing structural evolution of Cu-SAC-NC into nanograins. (AVI) Experimental details; supplementary spectra and fitting results of operando HERFD-XAS and EXAFS; additional TEM, SEM, STEM, and XPS characterizations; in situ ATR-SEIRAS spectroscopy; operando EC-STEM images and 4D-STEM orientation analyses; comparison tables of CO₂RR performance and EXAFS fitting parameters; (PDF)

AUTHOR INFORMATION

Corresponding Authors

Yao Yang — Department of Chemistry and Chemical Biology, Baker Lab and Kavli Institute at Cornell for Nanoscale Science, Cornell University, Ithaca, New York 14853, United States; orcid.org/0000-0003-0321-3792; Email: yaoyang@cornell.edu

Jihye Park — Department of Chemistry, University of Colorado Boulder, Boulder, Colorado 80309, United States; Materials Science & Engineering Program, University of Colorado Boulder, Boulder, Colorado 80303, United States; Orcid.org/0000-0002-8644-2103; Email: jihye.park@colorado.edu

Yun Jeong Hwang — Department of Chemistry, College of Natural Sciences, Seoul National University (SNU), Seoul 08826, Republic of Korea; orcid.org/0000-0002-0980-1758; Email: yjhwang1@snu.ac.kr

Authors

- Juhyung Choi Department of Chemistry and Chemical Biology, Baker Lab, Cornell University, Ithaca, New York 14853, United States; orcid.org/0000-0003-0770-6113
- Sungin Kim Department of Chemistry and Chemical Biology, Baker Lab, Cornell University, Ithaca, New York 14853, United States; ⊙ orcid.org/0000-0001-9107-0781
- Ji Yong Choi Department of Chemistry, University of Colorado Boulder, Boulder, Colorado 80309, United States Sejin Park — Department of Chemistry, College of Natural
- Sejin Park Department of Chemistry, College of Natural Sciences, Seoul National University (SNU), Seoul 08826, Republic of Korea
- Kwanghwi Je Department of Chemistry and Chemical Biology, Baker Lab, Cornell University, Ithaca, New York 14853, United States
- Shikai Liu Department of Chemistry and Chemical Biology, Baker Lab, Cornell University, Ithaca, New York 14853, United States
- Jiahong Jiang Department of Chemistry and Chemical Biology, Baker Lab, Cornell University, Ithaca, New York 14853, United States; oorcid.org/0009-0004-8750-2560
- Shaojinlin Yang Department of Chemistry and Chemical Biology, Baker Lab, Cornell University, Ithaca, New York 14853, United States
- Christopher J. Pollock Cornell High Energy Synchrotron Source, Wilson Laboratory, Cornell University, Ithaca, New York 14853, United States; orcid.org/0000-0001-5736-513X
- Rafael Guzman-Soriano Department of Chemistry and Chemical Biology, Baker Lab, Cornell University, Ithaca, New York 14853, United States
- Kathryn Bairley Department of Chemistry, University of Colorado Boulder, Boulder, Colorado 80309, United States; orcid.org/0000-0003-0975-0652
- Bayu I. Z. Ahmad Department of Chemistry and Chemical Biology, Baker Lab, Cornell University, Ithaca, New York 14853, United States
- Phillip J. Milner Department of Chemistry and Chemical Biology, Baker Lab, Cornell University, Ithaca, New York 14853, United States; Occid.org/0000-0002-2618-013X
- Erik H. Thiede Department of Chemistry and Chemical Biology, Baker Lab, Cornell University, Ithaca, New York 14853, United States

Complete contact information is available at: https://pubs.acs.org/10.1021/jacs.5c14123

Author Contributions

¹J.C., S.K., J.Y.C., and S.P. contributed equally.

Notes

The authors declare no competing financial interest.

■ ACKNOWLEDGMENTS

This work was supported by the Cornell Atkinson Center for Sustainability and the 2030 Project: A Cornell Climate Initiative. We acknowledge the generous support from the Kavli Institute at Cornell (KIC) Instrumentation Grant. This work made use of TEM facilities at the Cornell Center for Materials Research (CCMR), which are supported through the National Science Foundation Materials Research Science and Engineering Center (NSF MRSEC) program (DMR-1719875). This work is based on research conducted at the Center for High-Energy X-ray Sciences (CHEXS), which is

supported by the National Science Foundation (BIO, ENG and MPS Directorates) under award DMR-2342336. We appreciate the dedicated support from John Grazul and Philip Carubia in maintaining the Perseus STEM for operando EC-STEM experiments at CCMR. J.C and S.K. are supported by the National Research Foundation of Korea (NRF) grant funded by the Korea government (MSIT) (RS-2024-00414454 and RS-2024-00351910, respectively). A section of this work used Delta and DeltaAI at the National Center for Supercomputing Applications through allocation CIS240889 from the Advanced Cyberinfrastructure Coordination Ecosystem: Services & Support (ACCESS) program, which is supported by U.S. National Science Foundation grants #2138259, #2138286, #2138307, #2137603, and #2138296. K.J. is supported by the Eric and Wendy Schmidt AI in Science Postdoctoral Fellowship, a program of Schmidt Sciences, LLC. This work was supported by the Korea Evaluation Institute of Industrial Technology (Alchemist Project, NTIS-2410013669, 20018904) through the Ministry of Trade, Industry and Energy, Korea. MOF catalysis studies were supported by the U.S. Department of Energy, Office of Science, Office of Basic Energy Sciences under Award Number DE-SC0024199 (B.I.Z.A., P.J.M.). We also acknowledge the support of a Camille Dreyfus Teacher-Scholar Award to P.J.M. (TC-23-048).

REFERENCES

- (1) Yang, Y.; Peltier, C. R.; Zeng, R.; Schimmenti, R.; Li, Q.; Huang, X.; Yan, Z.; Potsi, G.; Selhorst, R.; Lu, X. Electrocatalysis in alkaline media and alkaline membrane-based energy technologies. *Chem. Rev.* **2022**, *122* (6), 6117–6321.
- (2) Mefford, J. T.; Akbashev, A. R.; Kang, M.; Bentley, C. L.; Gent, W. E.; Deng, H. D.; Alsem, D. H.; Yu, Y.-S.; Salmon, N. J.; Shapiro, D. A. Correlative operando microscopy of oxygen evolution electrocatalysts. *Nature* **2021**, *593* (7857), 67–73.
- (3) Kim, S.; Briega-Martos, V.; Liu, S.; Je, K.; Shi, C.; Stephens, K. M.; Zeltmann, S. E.; Zhang, Z.; Guzman-Soriano, R.; Li, W.; et al. Operando Heating and Cooling Electrochemical 4D-STEM Probing Nanoscale Dynamics at Solid–Liquid Interfaces. *J. Am. Chem. Soc.* 2025, 147 (27), 23654–23671.
- (4) Yang, Y.; Louisia, S.; Yu, S.; Jin, J.; Roh, I.; Chen, C.; Fonseca Guzman, M. V.; Feijóo, J.; Chen, P.-C.; Wang, H. Operando studies reveal active Cu nanograins for CO₂ electroreduction. *Nature* **2023**, *614* (7947), 262–269.
- (5) Wu, Y.; Jiang, Z.; Lu, X.; Liang, Y.; Wang, H. Domino electroreduction of CO_2 to methanol on a molecular catalyst. *Nature* **2019**, 575 (7784), 639–642.
- (6) Hao, S.; Elgazzar, A.; Zhang, S.-K.; Wi, T.-U.; Chen, F.-Y.; Feng, Y.; Zhu, P.; Wang, H. Acid-humidified CO2 gas input for stable electrochemical CO₂ reduction reaction. *Science* **2025**, 388 (6752), No. eadr3834.
- (7) De Luna, P.; Hahn, C.; Higgins, D.; Jaffer, S. A.; Jaramillo, T. F.; Sargent, E. H. What would it take for renewably powered electrosynthesis to displace petrochemical processes? *Science* **2019**, 364 (6438), No. eaav3506.
- (8) Li, C. W.; Ciston, J.; Kanan, M. W. Electroreduction of carbon monoxide to liquid fuel on oxide-derived nanocrystalline copper. *Nature* **2014**, *508* (7497), 504–507.
- (9) Kim, I.; Lee, G.-B.; Kim, S.; Jung, H. D.; Kim, J.-Y.; Lee, T.; Choi, H.; Jo, J.; Kang, G.; Oh, S.-H.; et al. Unveiling the reconstruction of copper bimetallic catalysts during CO₂ electroreduction. *Nat. Catal.* **2025**, *8* (7), 697–713.
- (10) Lazouski, N.; Chung, M.; Williams, K.; Gala, M. L.; Manthiram, K. Non-aqueous gas diffusion electrodes for rapid ammonia synthesis from nitrogen and water-splitting-derived hydrogen. *Nat. Catal.* **2020**, 3 (5), 463–469.

https://doi.org/10.1021/jacs.5c14123 J. Am. Chem. Soc. XXXX, XXX, XXX—XXX

I

- (11) Fu, X.; Pedersen, J. B.; Zhou, Y.; Saccoccio, M.; Li, S.; Sažinas, R.; Li, K.; Andersen, S. Z.; Xu, A.; Deissler, N. H. Continuous-flow electrosynthesis of ammonia by nitrogen reduction and hydrogen oxidation. *Science* **2023**, *379* (6633), 707–712.
- (12) Yang, J.; Qi, H.; Li, A.; Liu, X.; Yang, X.; Zhang, S.; Zhao, Q.; Jiang, Q.; Su, Y.; Zhang, L. Potential-driven restructuring of Cu single atoms to nanoparticles for boosting the electrochemical reduction of nitrate to ammonia. *J. Am. Chem. Soc.* **2022**, 144 (27), 12062–12071.
- (13) Fairhurst, A. R.; Snyder, J.; Wang, C.; Strmcnik, D.; Stamenkovic, V. R. Electrocatalysis: From Planar Surfaces to Nanostructured Interfaces. *Chem. Rev.* **2025**, *125* (3), 1332–1419.
- (14) Yang, Y.; Xiong, Y.; Holtz, M. E.; Feng, X.; Zeng, R.; Chen, G.; DiSalvo, F. J.; Muller, D. A.; Abruña, H. D. Octahedral spinel electrocatalysts for alkaline fuel cells. *Proc. Natl. Acad. Sci. U. S. A.* **2019**, *116* (49), 24425–24432.
- (15) Trotochaud, L.; Young, S. L.; Ranney, J. K.; Boettcher, S. W. Nickel—iron oxyhydroxide oxygen-evolution electrocatalysts: the role of intentional and incidental iron incorporation. *J. Am. Chem. Soc.* **2014**, 136 (18), 6744–6753.
- (16) Choi, J.; Kim, D.; Zheng, W.; Yan, B.; Li, Y.; Lee, L. Y. S.; Piao, Y. Interface engineered NiFe₂O_{4-x}/NiMoO₄ nanowire arrays for electrochemical oxygen evolution. *Appl. Catal., B* **2021**, 286, 119857.
- (17) Kim, S.; Kwag, J.; Lee, M.; Kang, S.; Kim, D.; Oh, J.-G.; Heo, Y.-J.; Ryu, J.; Park, J. Unraveling Serial Degradation Pathways of Supported Catalysts through Reliable Electrochemical Liquid-Cell TEM Analysis. *J. Am. Chem. Soc.* **2025**, *147* (1), 181–191.
- (18) Harwood, S. J.; Palkowitz, M. D.; Gannett, C. N.; Perez, P.; Yao, Z.; Sun, L.; Abruña, H. D.; Anderson, S. L.; Baran, P. S. Modular terpene synthesis enabled by mild electrochemical couplings. *Science* **2022**, *375* (6582), 745–752.
- (19) Hoque, M. A.; Gerken, J. B.; Stahl, S. S. Synthetic dioxygenase reactivity by pairing electrochemical oxygen reduction and water oxidation. *Science* **2024**, 383 (6679), 173–178.
- (20) Choi, J.; Yoo, S.; Nguyen, P. M.; Lee, E.; Shin, H.; Hwang, Y. J. Phase Transition Kinetics via Operando Monitoring Electro-Oxidation Reaction of 5-Hydroxymethylfurfural on Amorphous Nickel Oxyhydroxide. *ACS Catal.* **2025**, *15* (9), 6906–6917.
- (21) Yang, Y.; Xiong, Y.; Zeng, R.; Lu, X.; Krumov, M.; Huang, X.; Xu, W.; Wang, H.; DiSalvo, F. J.; Brock, J. D. Operando methods in electrocatalysis. *ACS Catal.* **2021**, *11* (3), 1136–1178.
- (22) Yang, Y.; Feijóo, J.; Briega-Martos, V.; Li, Q.; Krumov, M.; Merkens, S.; De Salvo, G.; Chuvilin, A.; Jin, J.; Huang, H. Operando methods: A new era of electrochemistry. *Curr. Opin. Electrochem.* 2023, 42, 101403.
- (23) Yoon, A.; Bai, L.; Yang, F.; Franco, F.; Zhan, C.; Rüscher, M.; Timoshenko, J.; Pratsch, C.; Werner, S.; Jeon, H. S. Revealing catalyst restructuring and composition during nitrate electroreduction through correlated operando microscopy and spectroscopy. *Nat. Mater.* **2025**, 24 (5), 762–769.
- (24) Yang, Y.; Feijóo, J.; Figueras-Valls, M.; Chen, C.; Shi, C.; Fonseca Guzman, M. V.; Murhabazi Maombi, Y.; Liu, S.; Jain, P.; Briega-Martos, V. Operando probing dynamic migration of copper carbonyl during electrocatalytic CO₂ reduction. *Nat. Catal.* **2025**, 8 (6), 579–594.
- (25) Yang, Y.; Shi, C.; Feijóo, J.; Jin, J.; Chen, C.; Han, Y.; Yang, P. Dynamic evolution of copper nanowires during CO₂ reduction probed by operando electrochemical 4D-STEM and X-ray spectroscopy. *J. Am. Chem. Soc.* **2024**, *146* (33), 23398–23405.
- (26) Weng, Z.; Wu, Y.; Wang, M.; Jiang, J.; Yang, K.; Huo, S.; Wang, X.-F.; Ma, Q.; Brudvig, G. W.; Batista, V. S. Active sites of copper-complex catalytic materials for electrochemical carbon dioxide reduction. *Nat. Commun.* **2018**, *9* (1), 415.
- (27) Zhang, J.; My Pham, T. H.; Gao, Z.; Li, M.; Ko, Y.; Lombardo, L.; Zhao, W.; Luo, W.; Zuttel, A. Electrochemical CO2 reduction over copper phthalocyanine derived catalysts with enhanced selectivity for multicarbon products. *ACS Catal.* **2023**, *13* (14), 9326–9335.
- (28) Zhang, L.; Yang, X.; Yuan, Q.; Wei, Z.; Ding, J.; Chu, T.; Rong, C.; Zhang, Q.; Ye, Z.; Xuan, F.-Z. Elucidating the structure-stability relationship of Cu single-atom catalysts using operando surface-

- enhanced infrared absorption spectroscopy. Nat. Commun. 2023, 14 (1), 8311.
- (29) Hsu, C.-S.; Wang, J.; Chu, Y.-C.; Chen, J.-H.; Chien, C.-Y.; Lin, K.-H.; Tsai, L. D.; Chen, H.-C.; Liao, Y.-F.; Hiraoka, N. Activating dynamic atomic-configuration for single-site electrocatalyst in electrochemical CO₂ reduction. *Nat. Commun.* **2023**, *14* (1), 5245.
- (30) Xiao, X.; Gao, Y.; Zhang, L.; Zhang, J.; Zhang, Q.; Li, Q.; Bao, H.; Zhou, J.; Miao, S.; Chen, N. A promoted charge separation/transfer system from Cu single atoms and C₃N₄ layers for efficient photocatalysis. *Adv. Mater.* **2020**, 32 (33), 2003082.
- (31) Xu, P.; Bao, Z.; Zhao, Y.; Zheng, L.; Lv, Z.; Shi, X.; Wang, H. E.; Fang, X.; Zheng, H. Anionic Regulation and Heteroatom Doping of Ni-Based Electrocatalysts to Boost Biomass Valorization Coupled with Hydrogen Production. *Adv. Energy Mater.* **2024**, *14*, 2303557.
- (32) Chang, Q.; Liu, Y.; Lee, J.-H.; Ologunagba, D.; Hwang, S.; Xie, Z.; Kattel, S.; Lee, J. H.; Chen, J. G. Metal-coordinated phthalocyanines as platform molecules for understanding isolated metal sites in the electrochemical reduction of CO₂. *J. Am. Chem. Soc.* **2022**, *144* (35), 16131–16138.
- (33) Lu, T.; Shi, G.; Liu, Y.; Luo, X.; Shen, Y.; Chang, M.; Wu, Y.; Gao, X.; Wu, J.; Li, Y. Local Coordination Environment-Driven Structural Dynamics of Single-Atom Copper and the CO₂ Electroreduction Pathway. *J. Am. Chem. Soc.* **2025**, *147* (30), 26425–26436.
- (34) Chen, T.; Dou, J.-H.; Yang, L.; Sun, C.; Libretto, N. J.; Skorupskii, G.; Miller, J. T.; Dincă, M. Continuous electrical conductivity variation in M_3 (hexaiminotriphenylene)₂ (M= Co, Ni, Cu) MOF alloys. *J. Am. Chem. Soc.* **2020**, 142 (28), 12367–12373.
- (35) Gittins, J. W.; Balhatchet, C. J.; Chen, Y.; Liu, C.; Madden, D. G.; Britto, S.; Golomb, M. J.; Walsh, A.; Fairen-Jimenez, D.; Dutton, S. E. Insights into the electric double-layer capacitance of two-dimensional electrically conductive metal—organic frameworks. *J. Mater. Chem. A* **2021**, *9* (29), 16006—16015.
- (36) Wang, W.; Chen, B.; Guo, J.; Liu, Z.; Yuan, H.; Fan, B.; Huang, X. Fabrication of a Novel Cu Based Conjugated Coordination Polymer for Effective Electroreduction of Nitrate to Ammonia and Zn–Nitrate Batteries. *Adv. Funct. Mater.* **2025**, *35*, 2501057.
- (37) Sun, H.; Chen, L.; Xiong, L.; Feng, K.; Chen, Y.; Zhang, X.; Yuan, X.; Yang, B.; Deng, Z.; Liu, Y. Promoting ethylene production over a wide potential window on Cu crystallites induced and stabilized via current shock and charge delocalization. *Nat. Commun.* **2021**, *12* (1), 6823.
- (38) Pitt, T. A.; Azbell, T. J.; Kim, J.; Shi, Z.; Muller, D. A.; Addicoat, M. A.; Milner, P. J. A Strongly Reducing sp² Carbon-Conjugated Covalent Organic Framework Formed by N-Heterocyclic Carbene Dimerization. *Angew. Chem., Int. Ed.* **2025**, *64* (4), No. e202416480.
- (39) De Los Santos Valladares, L.; Salinas, D. H.; Dominguez, A. B.; Najarro, D. A.; Khondaker, S. I.; Mitrelias, T.; Barnes, C. H. W.; Aguiar, J. A.; Majima, Y. Crystallization and electrical resistivity of Cu_2O and CuO obtained by thermal oxidation of Cu thin films on SiO_2/Si substrates. Thin Solid Films 2012, 520 (20), 6368–6374.
- (40) Hämäläinen, K.; Siddons, D. P.; Hastings, J. B.; Berman, L. E. Elimination of the inner-shell lifetime broadening in x-ray-absorption spectroscopy. *Phys. Rev. Lett.* **1991**, *67* (20), 2850–2853.
- (41) Glatzel, P.; Bergmann, U. High resolution 1s core hole X-ray spectroscopy in 3d transition metal complexes—electronic and structural information. *Coord. Chem. Rev.* **2005**, 249 (1), 65–95.
- (42) Feijóo, J.; Yang, Y.; Fonseca Guzman, M. V.; Vargas, A.; Chen, C.; Pollock, C. J.; Yang, P. Operando High-Energy-Resolution X-ray Spectroscopy of Evolving Cu Nanoparticle Electrocatalysts for CO₂ Reduction. *J. Am. Chem. Soc.* **2023**, *145* (37), 20208–20213.
- (43) Debela, T. T.; Hendon, C. H. Hydrogenic Defects in Ferromagnetic $Cu_3(HITP)_2$ (HITP $\equiv 2,3,6,7,10,11$ -Hexaiminotriphenylene), a 2D Metal–Organic Framework. ACS Mater. Lett. **2024**, 6 (7), 2698–2702.
- (44) Yang, J.; Liu, W.; Xu, M.; Liu, X.; Qi, H.; Zhang, L.; Yang, X.; Niu, S.; Zhou, D.; Liu, Y.; et al. Dynamic Behavior of Single-Atom Catalysts in Electrocatalysis: Identification of Cu-N₃ as an Active Site

- for the Oxygen Reduction Reaction. J. Am. Chem. Soc. 2021, 143 (36), 14530-14539.
- (45) Yokoyama, T.; Kosugi, N.; Kuroda, H. Polarized xanes spectra of $CuCl_2 \cdot 2H_2O$. Further evidence for shake-down phenomena. *Chem. Phys.* **1986**, *103* (1), 101–109.
- (46) Hursán, D.; Timoshenko, J.; Ortega, E.; Jeon, H. S.; Rüscher, M.; Herzog, A.; Rettenmaier, C.; Chee, S. W.; Martini, A.; Koshy, D.; et al. Reversible Structural Evolution of Metal-Nitrogen-Doped Carbon Catalysts During CO₂ Electroreduction: An Operando X-ray Absorption Spectroscopy Study. *Adv. Mater.* **2024**, *36* (4), 2307809.
- (47) Vavra, J.; Ramona, G. P. L.; Dattila, F.; Kormányos, A.; Priamushko, T.; Albertini, P. P.; Loiudice, A.; Cherevko, S.; Lopéz, N.; Buonsanti, R. Solution-based Cu⁺ transient species mediate the reconstruction of copper electrocatalysts for CO₂ reduction. *Nat. Catal.* **2024**, *7* (1), 89–97.
- (48) Moradzaman, M.; Mul, G. Infrared Analysis of Interfacial Phenomena during Electrochemical Reduction of CO₂ over Polycrystalline Copper Electrodes. *ACS Catal.* **2020**, *10* (15), 8049–8057.
- (49) Dunwell, M.; Yan, Y.; Xu, B. A surface-enhanced infrared absorption spectroscopic study of pH dependent water adsorption on Au. Surf. Sci. 2016, 650, 51–56.
- (50) Wu, R. C.; Liu, D.; Geng, J. Z.; Bai, H. Y.; Li, F. F.; Zhou, P. F.; Pan, H. Electrochemical Reduction of CO₂ on Single-Atom Catalysts Anchored on N-Terminated TiN (111): Low Overpotential and High Selectivity. *Appl. Surf. Sci.* **2022**, *602* (15), 154239.
- (51) Wu, J.; Chen, Y.; Du, W.; Hao, Y.; Wang, S.; Wang, R.; Cha, S.; Yang, X.; Yan, C.; Lian, C.; Liu, H.; Gong, M. Concentrated Zwitterion Interfaces for Selective Promotion of Electrochemical Hydroxide Oxidation. *J. Am. Chem. Soc.* **2025**, *147* (36), 32717–32728.
- (52) Tao, H.; Wang, S.; Liu, H.; Lian, C. Deep Neural Network Enhanced Mesoscopic Thermodynamic Model for Unlocking the Electrode/Electrolyte Interface. *Angew. Chem., Int. Ed.* **2025**, *64* (6), No. e202418447.
- (53) Lian, C.; Janssen, M.; Liu, H.; van Roij, R. Blessing and Curse: How a Supercapacitor's Large Capacitance Causes Its Slow Charging. *Phys. Rev. Lett.* **2020**, *124*, No. 076001.
- (54) Tate, M. W.; Purohit, P.; Chamberlain, D.; Nguyen, K. X.; Hovden, R.; Chang, C. S.; Deb, P.; Turgut, E.; Heron, J. T.; Schlom, D. G.; et al. High Dynamic Range Pixel Array Detector for Scanning Transmission Electron Microscopy. *Microsc. Microanal.* **2016**, 22 (1), 237–249.
- (55) Yang, Y.; Shao, Y.-T.; Lu, X.; Yang, Y.; Ko, H.-Y.; DiStasio, R. A., Jr.; DiSalvo, F. J.; Muller, D. A.; Abruña, H. D. Elucidating Cathodic Corrosion Mechanisms with Operando Electrochemical Transmission Electron Microscopy. *J. Am. Chem. Soc.* **2022**, *144* (34), 15698–15708.
- (56) Kim, J.; Rhee, J.; Kang, S.; Jung, M.; Kim, J.; Jeon, M.; Park, J.; Ham, J.; Kim, B. H.; Lee, W. C.; Roh, S.-H.; Park, J.; et al. Self-supervised machine learning framework for high-throughput electron microscopy. *Sci. Adv.* **2025**, *11* (14), No. eads5552.
- (57) Ophus, C.; Zeltmann, S. E.; Bruefach, A.; Rakowski, A.; Savitzky, B. H.; Minor, A. M.; Scott, M. C. Automated Crystal Orientation Mapping in py4DSTEM using Sparse Correlation Matching. *Microsc. Microanal.* **2022**, 28 (2), 390–403.
- (58) Boerner, T. J.; Deems, S.; Furlani, T. R.; Knuth, S. L.; Towns, J. ACCESS: Advancing Innovation: NSF's Advanced Cyberinfrastructure Coordination Ecosystem: Services and Support. Practice and Experience in Advanced Research Computing 2023: Computing for the Common Good-PEARC23, Portland, OR, July 23–27, 2023, ACM, 2023; pp 173–176.



CAS BIOFINDER DISCOVERY PLATFORM™

BRIDGE BIOLOGY AND CHEMISTRY FOR FASTER ANSWERS

Analyze target relationships, compound effects, and disease pathways

Explore the platform

